Instabilities and inertial waves generated in a librating cylinder

J. M. Lopez[1,2]† and F. Marques[3]

[1] School of Mathematical and Statistical Sciences, Arizona State University, Tempe, AZ 85287, USA

[2] Department of Mathematics, Kyungpook National University, Daegu 702-701, Republic of Korea

[3] Departament de Física Aplicada, Universitat Politècnica de Catalunya, Barcelona 08034, Spain

A librating cylinder consists of a rotating cylinder whose rate of rotation is modulated. When the mean rotation rate is large compared with the viscous damping rate, the flow may support inertial waves, depending on the frequency of the modulation. The modulation also produces time-dependent boundary layers on the cylinder endwalls and sidewall, and the sidewall boundary layer flow in particular is susceptible to instabilities which can introduce additional forcing on the interior flow with time scales different from the modulation period. These instabilities may also drive and/or modify the inertial waves. In this paper, we explore such flows numerically using a spectral-collocation code solving the Navier–Stokes equations in order to capture the dynamics involved in the interactions between the inertial waves and the viscous boundary layer flows.

1. Introduction

Longitudinal librations refer to torsional oscillations about the axis of a rotating axisymmetric fluid-filled cavity. There has been, and continues to be, much interest in these flows motivated by issues in planetology (Aldridge & Lumb 1987; Zatman & Bloxham 1997; Noir *et al.* 2009; Calkins *et al.* 2010; Noir *et al.* 2010). The scales involved in planetary hydrodynamics present grand challenges to theoretical and numerical modelling, and the need for compromises in laboratory-scale experiments designed to investigate such flows. The rapid background rotation leads to an interior flow very close to solid-body rotation that is capable of sustaining inertial waves (Aldridge & Toomre 1969; Aldridge & Lumb 1987), and at the same time the differential rotation due to the torsional oscillations lead to the formation of thin boundary layers on the container walls. Based on their experimental study of librations of rotating spherical shells, Noir *et al.* (2009) argue that the observed instabilities near the equator in the outer sphere's boundary layer are primarily driven by a local centrifugal instability during the retrograde phase of the outer sphere's oscillation. Busse (2010*a*) presents an asymptotic analysis of the librating spherical cavity problem, considering the limit of small amplitude and frequency of the torsional oscillations. He shows that a mean zonal flow results from a geostrophic response

† Email address for correspondence: juan.m.lopez@asu.edu

generated via nonlinearities in the boundary layers, and argues that this mean flow may play an essential role in the generation of the observed longitudinal rolls. Neither of these recent investigations consider the role of inertial waves in the transition to observed 'wavy' turbulence.

While these recent studies on librating flows have been motivated by planetary problems, these types of flows have also attracted considerable interest from a flow instability control perspective, particularly in rotating convection problems (Bhattacharjee 1989, 1990; Niemela, Smith & Donnelly 1991; Thompson, Bajaj & Ahlers 2002; Roxin & Riecke 2002; Rubio, Lopez & Marques 2008, 2009). Further, librating cylinder flows, with additional differential rotation, have also been employed to study the fundamental dynamics of wind-forced ocean gyres (Hart & Mundt 1996).

The experiments of Noir *et al.* (2009) show that the onset of laminar longitudinal rolls and the onset of their transition to turbulence occur at well-characterized critical values of the boundary layer Reynolds number, over about a decade of background rotation (the range being limited by the mechanics of their apparatus). As well as the spherical cavity problems, they also report on some preliminary observations in a torsionally oscillated rotating cylinder, i.e. a librating cylinder, showing the presence of longitudinal roll structures throughout the sidewall boundary layer.

In a subsequent study (Noir *et al.* 2010), they presented more details of the librating cylinder experiment where they noted that the transition to wavy turbulence is abrupt. It is this flow that we investigate in detail in this paper. Busse (2010*b*) also considered this type of flow, but in the limit that the modulation frequency is very much smaller than the mean rotation frequency of the cylinder, and in an asymptotic limit where the radius is much larger than the height of the cylinder such that the sidewall layer is omitted from the analysis. From the analysis of linear transient spin-up and spin-down, Greenspan & Howard (1963) suggest that the sidewall layer is passive, however Barcilon (1968) suggests that this may not be the case. The analysis of Barcilon (1968) is still linear and does not consider fully coupled horizontal and vertical boundary layers via the corner region, although he does discuss some aspects of the corner region flow. The main result from the asymptotic analysis of Busse (2010*b*) is that a mean retrograde interior zonal flow is produced whose magnitude scales with the modulation amplitude squared. However, the analysis of Wang (1970), which does include sidewall boundary layer considerations as well as the corners where the horizontal and sidewall layers meet, already established this result and confirmed the analysis with an experiment.

Rubio *et al.* (2009) also considered a librating cylinder flow in the low modulation amplitude limit, but within a fully nonlinear Navier–Stokes formulation that also accounted for the nonlinear coupling between the horizontal and sidewall boundary layers. They found that a mean retrograde zonal flow is produced whose magnitude scales with the modulation amplitude squared, and showed that this scaling comes naturally from the harmonic nature of the modulation. Further, they noted that the strength of this mean zonal flow is greatest at the sidewall. Their study also included thermal convection, but the results about the mean zonal flows were in a regime below the onset of convection where the temperature field may be expected to act as a passive scalar.

The experiments of Noir *et al.* (2010) also report a mean retrograde zonal flow whose magnitude scales with the modulation amplitude squared, and their results are not limited to very small modulation amplitudes. They also comment on the presence of inertial waves since the modulation frequencies they impose are typically less than twice the background rotation frequency, but they do not present direct measurements

of these waves. At the larger amplitudes, they find that the sidewall layer is unstable to Taylor–Görtler-type vortices which abruptly become wavy turbulent with a very small further increase in modulation amplitude.

There have been several studies of boundary layer flows with a fast background rotation where the boundary has been subjected to torsional oscillations, including the torsional oscillation of a rotating infinite unbounded disc (Benney 1965; Jones 1969), the torsional oscillation of two infinite discs (Barrett 1969), as well as the boundary layer analysis of the torsional oscillations of an enclosed rotating cylinder (Wang 1970). This last case corresponds to the geometry considered in this paper. In all of these problems, the boundary layer equations develop a singularity when the (torsional) modulation frequency is twice the background rotation frequency. This so-called resonant breakdown comes about as the boundary layer thickness becomes ill-defined at this frequency ratio, with the boundary layer flow extending deep into the interior. It is significant that it is for this frequency ratio and smaller that inertial waves are possible in the interior. Wang (1970) also conducted some laboratory experiments in the librating cylinder, confirming his theoretical prediction of a mean azimuthal bulk flow that scales with the modulation amplitude squared and the modulation frequency. Wang noted that when the modulation frequency is less than twice the background rotation frequency, the scatter in the experimental measurements of the mean flow were larger than that found for larger modulation frequencies. He concluded that this must be due to the presence of inertial waves, even though the modulation amplitudes used were very small.

In this study we explore in § 3 the boundary layer structure of the base state and the presence of inertial waves when the modulation frequency is smaller than twice the background rotation frequency Ω, and also an axisymmetric period doubling bifurcation that is able to excite inertial waves for modulation frequencies larger than 2Ω. In § 4 we explore the three-dimensional states that appear when the base state loses stability on increasing the modulation amplitude, and the wavy turbulent states that appear close to the bifurcation, for different values of the modulation frequency.

2. Governing equations and numerical methods

Consider the flow in a circular cylinder of radius R and height H, completely filled with a fluid of kinematic viscosity ν, rotating with a mean angular speed Ω that is harmonically modulated. A schematic of the flow system is shown in figure 1. The Navier–Stokes equations, non-dimensionalized using R as the length scale and $1/\Omega$ as the time scale, are

$$(\partial_t + \boldsymbol{u} \cdot \boldsymbol{\nabla})\boldsymbol{u} = -\boldsymbol{\nabla} p + \frac{1}{Re}\nabla^2 \boldsymbol{u}, \quad \boldsymbol{\nabla} \cdot \boldsymbol{u} = 0, \tag{2.1}$$

where $\boldsymbol{u} = (u, v, w)$ is the velocity field in polar coordinates $(r, \theta, z) \in [0, 1] \times [0, 2\pi] \times [-\gamma/2, \gamma/2]$ and p is the kinematic pressure. The boundary conditions are no-slip: on the cylinder sidewall $(u, v, w) = (0, 1 + \alpha \sin \omega t, 0)$, on the top and bottom endwalls $(u, v, w) = (0, r(1 + \alpha \sin \omega t), 0)$. There are four governing parameters:

$$
\begin{aligned}
&\text{Reynolds number,} &&Re = \Omega R^2/\nu; \\
&\text{aspect ratio,} &&\gamma = H/R; \\
&\text{modulation amplitude,} &&\alpha; \\
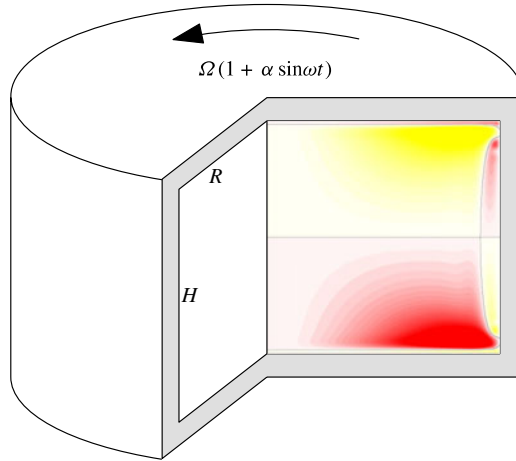&\text{modulation frequency,} &&\omega.
\end{aligned}
\tag{2.2}
$$

FIGURE 1. (Colour online available at journals.cambridge.org/flm) Schematic of the apparatus including streamfunction contours of a basic state at $Re = 10^4$, $\gamma = 1.0$, $\alpha = 0.5$ and $\omega = 0.8\pi$.

Present study	Wang (1970)	Rubio *et al.* (2009)	Busse (2010*b*)	Noir *et al.* (2010)
Re	$\alpha^2\beta/\epsilon$	$\Omega_0\gamma^2$	R^2/E	$1/E$
γ	$1/\alpha$	$1/\gamma$	$1/R$	2χ
α	$\delta/2\beta$	A	ϵ	ϵ
ω	$1/\beta$	Ω_m/Ω_0	ω	f

TABLE 1. The parameters used in the present study are given as a function of the parameters used in other studies.

Study	γ	Re	α	ω
Present study	1	10^4	[0.2, 0.9]	[1.2, 2.6]
Wang (1970), experiments	2.26	$[0.39, 14] \times 10^4$	[0.14, 13.0]	[1.0, 100]
Rubio *et al.* (2009)	0.25	10^4	[0.0, 0.05]	[0.0, 1.6]
Noir *et al.* (2010)	2.14	$[0.1, 10.0] \times 10^4$	[0.0, 5.0]	[0.1, 3.0]
Wang (1970), theory	~ 1	Asymptotics: $\alpha \ll (\omega/Re)^{1/2} \ll \omega$.		
Busse (2010*b*)	~ 0	Asymptotics: $Re^{-1/2} \ll \omega \ll 1$, $\alpha \ll 1$.		

TABLE 2. Parameter ranges used in different studies.

There are, of course, many different ways to non-dimensionalize the problem, and several of the previous studies on related problems have used different scalings. Table 1 gives the expression of the parameters used in the present study as a function of the parameters used in some of the other studies.

The present problem is governed by four non-dimensional independent parameters, and a comprehensive exploration of the parameter space is extremely expensive. Table 2 gives the parameter ranges explored in different studies. We have kept the

aspect ratio fixed at $\gamma = 1$ and the mean angular speed of the fluid container fixed at $Re = 10^4$; these are in the middle of the parameter ranges explored experimentally by other authors (as indicated in table 2). In this study, we have focused on the effects of the amplitude and frequency, α and ω, of the angular modulations. As the dynamics is mainly governed by the boundary layers appearing at the container walls, and the boundary layer thickness is much smaller than the dimensions of the cylinder, it is reasonable to assume that changing the aspect ratio does not qualitatively change the dynamics, as the previous studies suggest. Inertial waves may appear for $\omega \leqslant 2$, so we have explored a range of the modulation frequency around 2. For the modulation amplitude, we have selected values able to excite inertial waves with enough amplitude to be detected, but not too large, because the flow becomes turbulent at large amplitudes, i.e. we consider $\alpha \lesssim 1$.

The governing equations and boundary conditions are invariant under arbitrary rotations through angle ϕ about the axis, R_ϕ, whose action is

$$R_\phi(u, v, w)(r, \theta, z, t) = (u, v, w)(r, \theta + \phi, z, t). \tag{2.3}$$

They are also reflection-symmetric about the cylinder half-height. The action K_z of this symmetry is

$$K_z(u, v, w)(r, \theta, z, t) = (u, v, -w)(r, \theta, -z, t). \tag{2.4}$$

The symmetry group of the system is $G = SO(2) \times Z_2$, with $SO(2)$ generated by R_ϕ and Z_2 by K_z.

The governing equations (2.1) have been solved using a second-order time-splitting method, with space discretized via a Galerkin–Fourier expansion in θ and Chebyshev collocation in r and z. The spectral solver is based on that described by Mercader, Batiste & Alonso (2010) and it has recently been tested and used in a wide variety of enclosed cylinder flows (Marques *et al.* 2007; Lopez *et al.* 2007; Lopez & Marques 2009; Lopez *et al.* 2009; Do, Lopez & Marques 2010; Lopez & Marques 2010). For the solutions presented here, with $\gamma = 1$, we have used up to $n_r = n_z = 64$ Chebyshev modes in the radial and axial directions and up to $n_\theta = 128$ azimuthal Fourier modes. Typically, we have used 2500 time steps per modulation period $\tau = 2\pi/\omega$. The viscous time is R^2/ν, so that in non-dimensional time units, the viscous time is Re, and for the range of modulation frequencies considered, there are a few thousand periods per viscous time (i.e. $\omega Re/2\pi$ modulation, or libration, periods per viscous time unit).

3. Synchronous, axisymmetric basic state

Since the synchronous state is axisymmetric, it is convenient to describe it in terms of streamlines and vortex lines. The meridional components of velocity can be written in terms of the Stokes streamfunction, $u = -1/r \, \partial \psi/\partial z$ and $w = 1/r \, \partial \psi/\partial r$ and the vorticity is

$$\nabla \times \boldsymbol{u} = (\xi, \eta, \zeta) = \left(-\frac{1}{r} \frac{\partial rv}{\partial z}, -\frac{1}{r} \left(\frac{\partial^2}{\partial r^2} - \frac{1}{r} \frac{\partial}{\partial r} + \frac{\partial^2}{\partial z^2} \right) \psi, \frac{1}{r} \frac{\partial rv}{\partial r} \right). \tag{3.1}$$

Contours of ψ in a meridional plane depict the streamlines, and likewise, contours of rv depict the vortex lines. Note that ψ and η are independent of the rotating frame of reference; we compute and present results mainly in the inertial (i.e. stationary) frame of reference, although the velocity and vorticity fields are the same in both the inertial frame and the frame rotating with mean angular velocity Ω, except for
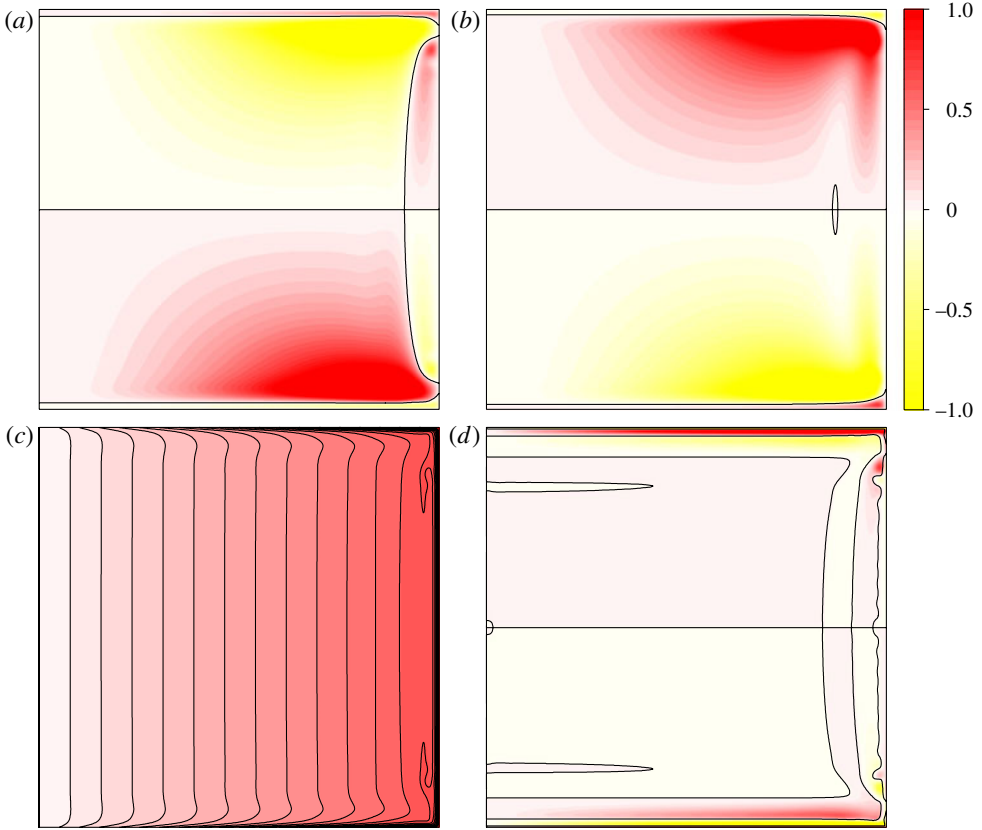
FIGURE 2. (Colour online) Contours of ψ, v and η at the phases as indicated, for the $SO(2) \times Z_2$ state at $Re = 10^4$, $\gamma = 1.0$, $\alpha = 0.5$ and $\omega = 0.8\pi \approx 2.513 > 2$. The colour bar is scaled by the maximum (red) and minimum (yellow) levels of each variable with $\psi \in [-0.0005, 0.0005]$, $v \in [0.0, 1.5]$, and $\eta \in [-5.0, 5.0]$: (a) ψ at 0.25τ; (b) ψ at 0.75τ; (c) v at 0.25τ; (d) η at 0.25τ.

the azimuthal velocity ($v = v_{rot} + r$) and the axial vorticity ($\zeta = \zeta_{rot} + 2$), where the subscript $_{rot}$ refers to the mean rotating frame; using the mean rotating frequency Ω as the time scale, the non-dimensional form of Ωr is just r.

In the unmodulated problem, with $\alpha = 0$, the fluid remains in solid-body rotation with vortex lines parallel to the rotation axis. Figure 2 shows the streamlines, azimuthal velocity and azimuthal vorticity of a periodic solution at $Re = 10^4$, $\gamma = 1.0$, $\alpha = 0.5$ and $\omega = 0.8\pi$ at one phase in time. This is the basic state; it is axisymmetric, reflection symmetric and synchronous with the forcing. The most salient features of the base state are the presence of time-dependent boundary layers at the top and bottom endwalls and the sidewall, and the presence of a large-scale circulation (LSC) emanating from the corners. The velocity field changes sign in the LSC region away from the sidewall every half period, as shown in the streamline plots in figure 2. However, the circulation close to the sidewall (SWC) always has the same sign.

Figure 3 shows the tangential (radial and azimuthal) velocity profiles at the top endwall boundary layer at the midradius ($r = 0.5$). Both oscillate in time and decay exponentially fast towards the interior of the fluid, as can be seen from the 10 profiles (grey) equally spaced over a forcing period τ. The blue and red profiles correspond to the maximum (at $t = \tau/4$) and minimum (at $t = 3\tau/4$) angular velocities of the
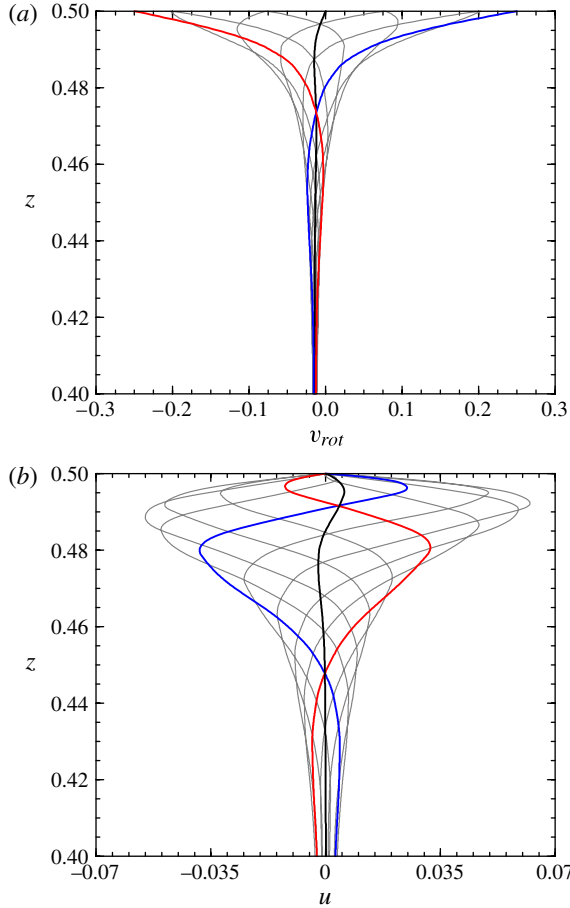
FIGURE 3. (Colour online) Velocity profiles in the top boundary layer, for the $SO(2) \times Z_2$ state at $Re = 10^4$, $\gamma = 1.0$, $\alpha = 0.5$ and $\omega = 0.8\pi$, the same state as in figure 2; (*a*) shows the azimuthal velocity v_{rot} in the rotating frame and (*b*) shows the radial velocity u. Ten equispaced profiles in a forcing period are plotted, at the radial location $r = 0.5$; the blue and red profiles correspond to $t = \tau/4$ and $t = 3\tau/4$. The black profile is the time-averaged velocity.

cylindrical container. The time average of these profiles is not zero, and the thick black curves in figure 3 show the time averages $\bar{u}$ and $\bar{v}_{rot}$, where we have defined $\bar{f} = 1/\tau \int_{t_0}^{t_0+\tau} f(t) \, \mathrm{d}t$. For synchronous solutions, $\bar{f}$ is independent of t_0, but this is not the case for more general non-periodic solutions and time averages must be taken over several periods in order to obtain results whose dependence on t_0 is very small.

A comprehensive analysis of boundary layers and inertial waves in rotating fluids is presented in Greenspan (1968), where steady and unsteady situations were considered. The particulars of the finite enclosed cylindrical geometry and the periodic forcing, as used in the present problem, were elaborated on in great detail by Wang (1970), and only minor particular additional results have been incorporated in subsequent studies (Yih 1977; Rubio *et al.* 2009; Busse 2010*b*). In order to compare the boundary layer structure of the base state that we have numerically computed with the theory from Wang (1970), the computed velocity field $\boldsymbol{u}$ is separated into a steady part, i.e. the time-averaged $\bar{\boldsymbol{u}}$, and an unsteady part $\tilde{\boldsymbol{u}} = \boldsymbol{u} - \bar{\boldsymbol{u}}$ with zero temporal mean, i.e. a purely oscillatory part. The unsteady boundary layer profiles at the top and bottom endwalls
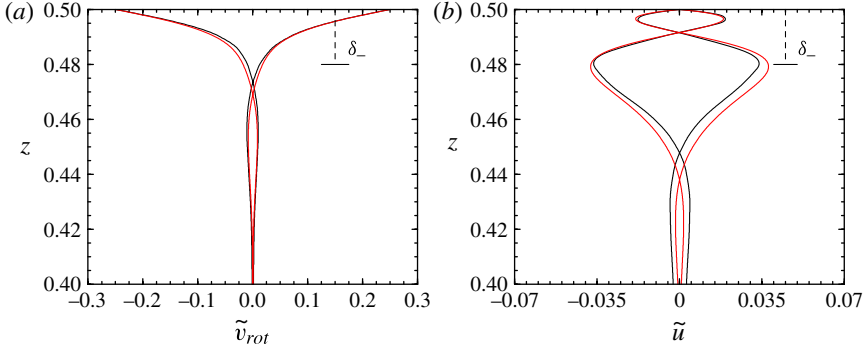
FIGURE 4. (Colour online) Velocity profiles in the top boundary layer, for the $SO(2) \times Z_2$ state at $Re = 10^4$, $\gamma = 1.0$, $\alpha = 0.5$ and $\omega = 0.8\pi$, the same state as in figure 2; (*a*) shows the unsteady azimuthal velocity $\tilde{v}_{rot}$ in the rotating frame and (*b*) shows the unsteady radial velocity $\tilde{u}$, at the radial location $r = 0.5$; the black profiles are computed numerically, and the red profiles are given by Wang (1970), (3.2) and (3.3).

obtained by Wang, in terms of the parameters used in the present study, are given by

$$\tilde{u} = \tfrac{1}{2}\alpha r(e^{-\tilde{z}/\delta_+}\cos(\omega t - \tilde{z}/\delta_+) - e^{-\tilde{z}/\delta_-}\cos(\omega t - s\tilde{z}/\delta_-)), \qquad (3.2)$$

$$\tilde{v}_{rot} = \tfrac{1}{2}\alpha r(e^{-\tilde{z}/\delta_+}\sin(\omega t - \tilde{z}/\delta_+) + e^{-\tilde{z}/\delta_-}\sin(\omega t - s\tilde{z}/\delta_-)), \qquad (3.3)$$

where $\tilde{z}$ is the z coordinate, but with origin at the endplate being considered, and pointing into the interior of the fluid, s is the sign of $\omega - 2$ (+1 if $\omega > 2$ and -1 if $\omega < 2$), and

$$\delta_+ = \sqrt{\frac{2}{(\omega + 2)Re}}, \qquad \delta_- = \sqrt{\frac{2}{|\omega - 2|Re}}. \qquad (3.4)$$

A measure of the boundary layer thickness is given by the largest of $\delta_\pm$, i.e. by δ_-. Figure 4 shows the numerically computed unsteady parts of the velocities in figure 3, $\tilde{u} = u - \bar{u}$ (black curves) together with Wang's profiles, (3.2) and (3.3) (red curves). The agreement is very good, considering that Wang's results are valid for $\alpha/\omega \ll (\omega Re)^{-1/2} \ll 1$. In the numerical case considered in the figure, $(\omega Re)^{-1/2} \approx 6 \times 10^{-3}$, but the forcing amplitude $\alpha/\omega \approx 0.2$ is quite large. Wang (1970)'s profiles are antisymmetric, in the sense that $\tilde{u}(t + \tau/2) = -\tilde{u}(t)$; the computed profiles show small deviations from this behaviour, i.e. they are not purely sinusoidal, due to the presence of harmonics ($2\omega t$, $3\omega t$, etc.) generated by the nonlinear terms in the Navier–Stokes equations. The boundary layer thickness estimate $\delta_- \approx 0.0197$ is also plotted. The boundary layers at the top and bottom endwalls are identical because the base flow is reflection symmetric. These endwall boundary layers are a combination of the Ekman boundary layer and the Stokes boundary layer (see Schlichting & Gersten 2000, Stokes' second problem).

The mean azimuthal velocity does not go to zero away from the boundary layer, but is slightly negative (retrograde), as can be seen in figure 3(*a*). In fact, the bulk of the fluid is in solid-body rotation, but with a small retrograde precession (angular translation) in the rotating frame, whose value in the case considered in the aforementioned figure is $\Omega_p \approx -0.0285$. Wang (1970) found the precession frequency of the bulk as a function of ω, and also measured it experimentally, with good agreement; the result he reports for the case considered here is $\Omega_p \approx -0.0309$, in good

agreement with our numerical result, considering that the amplitude $\alpha = 0.5$ is larger than that used in Wang's experiments ($\alpha = 0.34$). We have extracted these values from figure 2 in Wang's paper, where $\Omega'(\beta)$ is given; the relationship with our parameters is $\beta = 1/\omega$ and $\Omega_p = \alpha^2 \Omega'/\omega$. Therefore, the precession frequency of the bulk varies quadratically with the amplitude α of the forcing, a fact also reported by Rubio *et al.* (2009) and Busse (2010*b*).

Apart from the tangential velocities, u and v, there is a small axial velocity component w in the boundary layer, very similar to the pumping velocity typical of Ekman boundary layers. It can be easily computed from the continuity equation, resulting in $w = -\int_0^{\tilde{z}} 1/r \partial_r (ru) \, \mathrm{d}\tilde{z}$; the exact expression can be obtained from (3.2), and it is of order $\alpha \delta_-$, much smaller than the tangential velocities that are of order α. This vertical axial velocity, combined with the radial velocity in the top and bottom boundary layers produces the oscillating LSC depicted in figure 2. This circulation emanates from the corner and is significant around the corner and close to the top and bottom boundary layers, penetrating into the bulk several boundary layer widths.

The sidewall boundary layer is more complex than the top and bottom boundary layers; the analysis of Wang (1970) describes it as consisting of three different layers for the steady mean flow field, but Wang does not describe the non-steady flow at all. Moreover, since the mean radial flow in the top (and bottom) boundary layer is positive (see figure 3*b*), there is a net injection of fluid into the sidewall boundary layer. Figure 5 shows the tangential velocities (azimuthal and axial) at the sidewall boundary layer, at $z = 3/8 \approx 0.37$, i.e. at $1/8$ of the cylinder length from the corner. Both oscillate in time and decay exponentially fast towards the interior of the fluid, as can be seen from the 10 profiles (grey) equispaced over a forcing period τ. The blue and red profiles correspond to the maximum (at $t = \tau/4$) and minimum (at $t = 3\tau/4$) angular velocities of the cylinder. The time average of these profiles is not zero, and the thick black curves in figure 5 show the time averages $\bar{v}_{rot}$ and $\bar{w}$. The azimuthal velocity profile has the same qualitative features as $\bar{v}_{rot}$ at the top boundary layer; however, the axial velocity profile is very different from the corresponding tangential component, $\bar{u}$. The mean axial velocity $\bar{w}$ (black curve in figure 5*b*) is large, and corresponds to a SWC zone that does not change sign with time, this can also be seen in figure 2. This recirculation zone is the result of the injection of fluid coming from the top and bottom boundary layers. The outer zone, where the velocities go to zero very slowly, corresponds to the LSC, discussed earlier, that changes sign every half forcing period. Also plotted in the figure are the three nested layer thicknesses estimated from Wang's analysis: (*a*) $\delta_3 = (Re)^{-1/4} \approx 0.10$, where the steady bulk precession Ω_p is brought to rest; (*b*) $\delta_2 = (Re)^{-1/3} \approx 0.046$, that balances the mass flux induced by the δ_3 layer; and (*c*) $\delta_1 = (\omega Re)^{-1/2} \approx 0.0063$, the innermost layer, with a strong axial flow which accommodates the injected flow from the top endwall, and is important close to the corner. This axial flow decreases along the sidewall on approaching the cylinder midplane $z = 0$, where it becomes zero.

3.1. *Inertial waves*

For $\omega = 2$, i.e. when the forcing frequency is two times the mean angular speed of the container, the boundary layer thickness given by (3.3) grows unbounded, completely filling the container. This singularity coincides with the appearance of inertial waves. These waves are typical of rotating flows (Greenspan 1968); they are excited by changes in the angular velocity of the container and decay rapidly, but continuous changes of the rotation rate (due to external noise or periodic forcing, or even due to intrinsic flow instabilities, say, in the boundary layers) can make them permanent. For
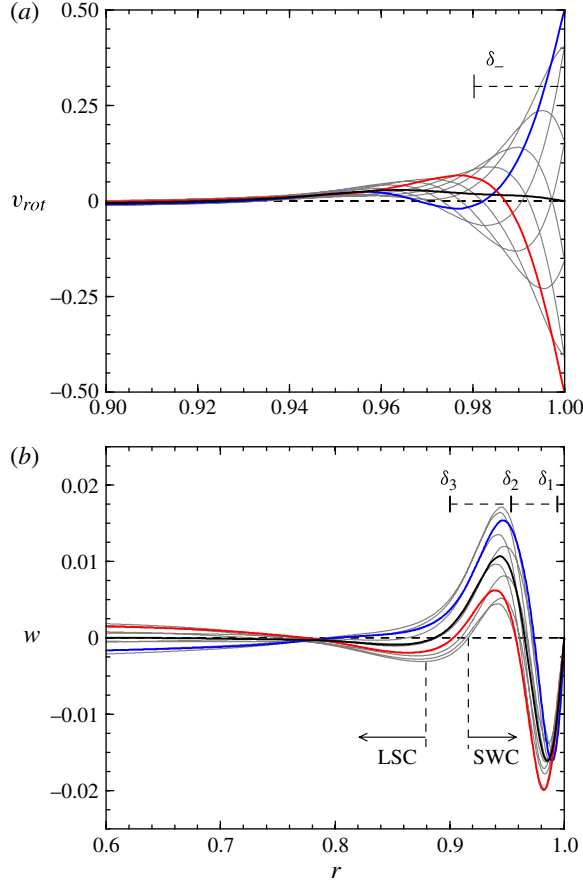
FIGURE 5. (Colour online) Velocity profiles in the sidewall boundary layer, for the $SO(2) \times Z_2$ state at $Re = 10^4$, $\gamma = 1.0$, $\alpha = 0.5$ and $\omega = 0.8\pi$, the same as in figure 2; (*a*) shows the azimuthal velocity v_{rot} in the rotating frame and (*b*) the vertical velocity w. Ten equispaced profiles in a forcing period are plotted, at the axial location $z = 0.37$; the blue and red profiles correspond to $t = \tau/4$ and $t = 3\tau/4$. The black profile is the time-averaged velocity.

periodically forced flows they only exist for $\omega \leqslant 2$, and the wave fronts make an angle given by $\cos\beta = \omega/2$ with the plane orthogonal to the rotation axis (see Landau & Lifshitz 1984, for a short and very clear discussion). These inertial waves change the nature and properties of the base flow, and although the boundary layer analysis, (3.2) and (3.3), can still be carried out for $\omega < 2$, it loses most of its meaning, due to the presence of the inertial waves. Of course, for small ω satisfying $1/\sqrt{Re} \ll \omega \ll 1$ it may be expected that their influence is negligible (Aldridge & Toomre 1969; Busse 2010*a,b*; Sauret *et al.* 2010).

   Figure 6 shows the streamlines, azimuthal velocity and azimuthal vorticity of a periodic solution at $Re = 10^4$, $\gamma = 1.0$, $\alpha = 0.2$ and $\omega = 0.6\pi \approx 1.885 < 2$ at one phase in time. By comparing with figure 2, there is a stark contrast between the flow structure in the $\omega > 2$ and the $\omega < 2$ cases. For $\omega < 2$, inertial waves play an important role, breaking the solid-body rotation of the bulk, establishing a time-dependent flow everywhere, and strongly modifying the boundary layers, that are now less intense. These states with inertial waves are still the basic state, axisymmetric and synchronous, for sufficiently small forcing amplitudes α; the presence of inertial waves is not an
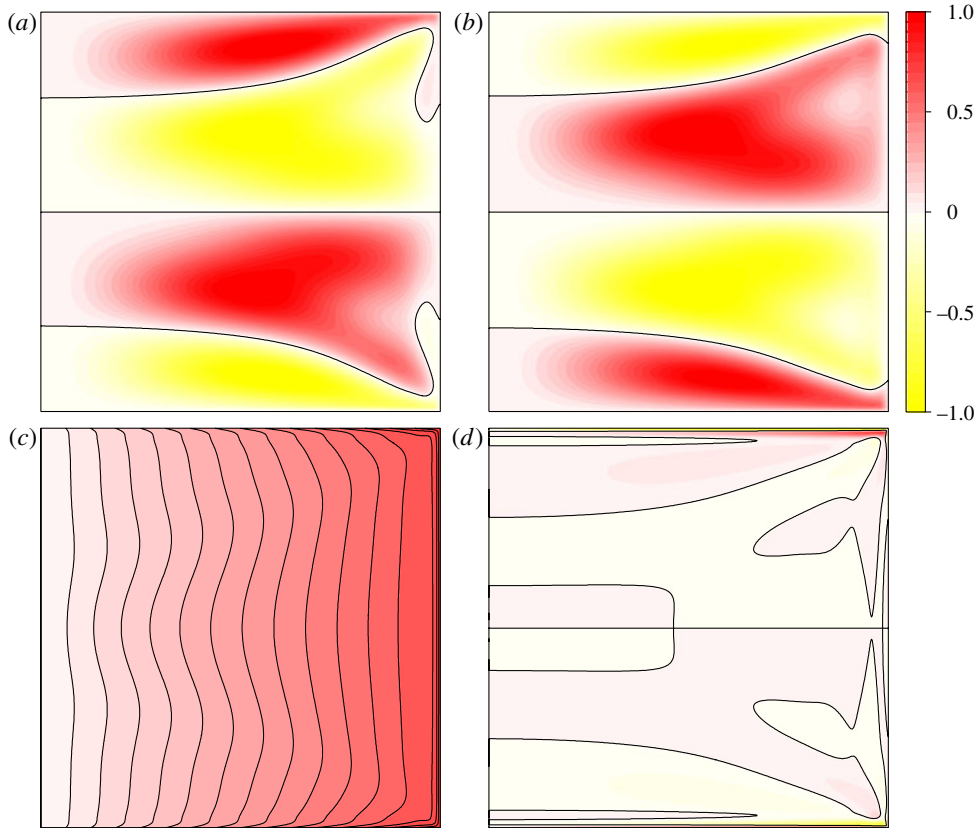
FIGURE 6. (Colour online) Contours of ψ, v and η at the phases as indicated, for the $SO(2) \times Z_2$ state at $Re = 10^4$, $\gamma = 1.0$, $\alpha = 0.2$ and $\omega = 0.6\pi \approx 1.885 < 2$. The colour bar is scaled by the maximum (red) and minimum (yellow) levels of each variable with $\psi \in [-0.0005, 0.0005]$, $v \in [0.0, 1.5]$ and $\eta \in [-5.0, 5.0]$: (*a*) ψ at 0.25τ; (*b*) ψ at 0.75τ; (*c*) v at 0.25τ; and (*d*) η at 0.25τ.

instability of the base state at a given modulation amplitude α_{crit}, but exist for all $\alpha > 0$, although their amplitude goes to zero linearly with α, for $\omega < 2$.

Even when $\omega > 2$, inertial waves can be generated via flow instabilities. We illustrate this with an example at $\omega = 0.8\pi$, which as we have shown earlier does not support inertial waves as long as α is sufficiently small (figure 2 showed such a case with $\alpha = 0.5$). By $\alpha = 0.75$ a number of subtle things happen, the flow remains axisymmetric and reflection symmetric about the midheight (i.e. $SO(2) \times Z_2$ symmetric), but now vortices form in the sidewall boundary layer symmetrically about the midheight and these equatorial vortices are not synchronous with the forcing. Instead, they oscillate at twice the forcing frequency; the flow has period doubled. The period doubling is quite localized to these equatorial vortices, the top and bottom endwall layers and the corner region appear to oscillate synchronously with the forcing (of course, on very much closer inspection, they too oscillate with their period doubled). The interesting result of this period doubling is that the flow now has a period of 0.4π, and so now the interior near-solid-body rotation flow has inertial waves and these propagate at an angle $\cos^{-1}(0.2\pi) \approx 51°$; figure 7 shows two snapshots of η exactly one forcing period apart.
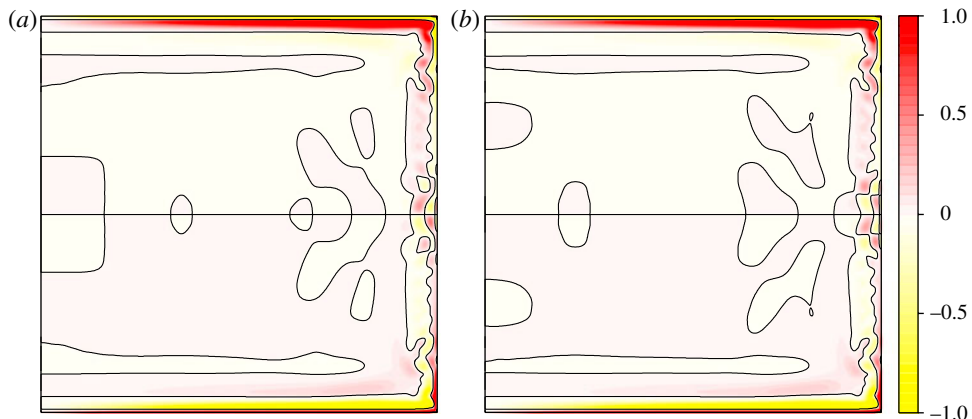
FIGURE 7. (Colour online) Contours of η at two phases exactly one forcing period apart, for the $SO(2) \times Z_2$ period-doubled state at $Re = 10^4$, $\gamma = 1.0$, $\alpha = 0.75$ and $\omega = 0.8\pi$. The colour bar is scaled by the maximum (red) and minimum (yellow) levels of $\eta \in [-5.0, 5.0]$: (a) 0.5τ; and (b) 1.5τ.

4. Three-dimensional flows

As the forcing amplitude α is increased, the basic state loses stability. How this occurs depends on the forcing frequency, ω, and there are a succession of secondary instabilities that occur over a small range of α leading to states with all symmetries broken and broadband temporal characteristics. These states resemble the wavy turbulent states observed in experiments (Noir *et al.* 2010). We have not performed a comprehensive bifurcation analysis of these cascades of instabilities as this would be a very expensive and challenging numerical exercise, but in the following we describe a number of the observed states for a few select values of ω and α illustrating the variety and complexity of the transitions to wavy turbulence.

In the previous section, we saw for $\omega = 0.8\pi$, a frequency value where the libration does not induce inertial waves in and of itself, that the centrifugal instability of the sidewall layer during the deceleration phase of the oscillation leads to the formation of vortices in the boundary layer, primarily about the cylinder half-height, and that these oscillate at half the forcing period and so induce inertial waves. This period-doubled flow at $\alpha = 0.75$ remains $SO(2) \times Z_2$ symmetric. On increasing α to 0.77, the vortices in the sidewall layer intensify and those in between the corner vortices and the vortices near the equator lose stability to azimuthal wavenumber $m = 3$ and the flow is now a modulated rotating wave state. Figure 8(a) shows the azimuthal vorticity on the sidewall, where the cylinder has been 'unwrapped' (i.e. plotting η on $r = 1.0$, $\theta \in [0, 2\pi]$, $z \in [0.0, 1.0]$). This snapshot in time illustrates that the corner vortices and the vortices at the equator are axisymmetric and the vortices in between break-up into a herringbone pattern. The two intense vortices about the equator are no longer mirror images of each other, the Z_2 reflection symmetry has also been broken. The inclined vortices have a mean precession and their intensity waxes and wanes with the cylinder libration.

Increasing the amplitude slightly to $\alpha = 0.80$, the form of the flow is the same, a modulated rotating wave, except that now the azimuthal wavenumber is $m = 4$. The plot of η on the sidewall, figure 8(b), and figure 9(a,b) showing η in a meridional section ($\theta = 0$) and a horizontal section ($z = 0.25$), illustrate that the Z_2 symmetry
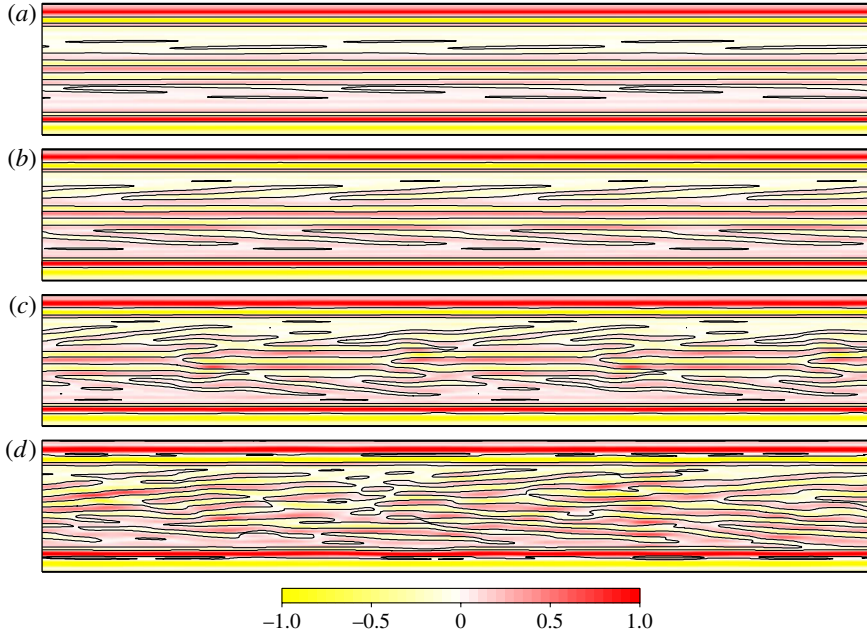
FIGURE 8. (Colour online) Azimuthal vorticity contours at $Re = 10^4$, $\gamma = 1.0$, $\omega = 0.8\pi$ with α as indicated, on the sidewall ($r = 1.0$, $\theta \in [0, 2\pi]$, $z \in [0.0, 1.0]$). The colour bar is scaled by the maximum (red) and minimum (yellow) levels of $\eta \in [-15, 15]$ (enhanced online): (*a*) $\alpha = 0.77$: (*b*) $\alpha = 0.80$; and (*c*) $\alpha = 0.82$; (*d*) $\alpha = 0.90$.

breaking is no longer localized to the sidewall vortices near the equator and that the non-axisymmetric flow is not localized to the vortices in between those at the equator and the corners; the interior flow has inertial waves that are not $SO(2) \times Z_2$.

Further increasing the amplitude to $\alpha = 0.82$ introduces an $m = 2$ azimuthal wavenumber, further modulating the modulated rotating wave. Energy is exchanged between $m = 2$ and $m = 4$ in an incommensurate fashion, as the online movie (available at journals.cambridge.org/flm) of η on the sidewall associated with figure 8 illustrates. The movie shows the mean precession of the sidewall vortices much better than in the lower α cases since at larger α, these vortices are more intense and persist throughout the entire libration cycle. One may view this persistence as a mean steady-streaming flow, but it is difficult to compute it unambiguously, not only because the flow is not time periodic, but because it is also non-axisymmetric and we do not have a very accurate estimate of the mean precession of the flow (if the time average is not done in a reference frame rotating exactly at the precession rate, large variabilities occur in estimates of a mean flow).

By $\alpha = 0.85$, the $m = 1$ azimuthal wavenumber has been excited and now the flow has all spatial and spatiotemporal symmetries broken; both spatial and temporal spectra are broadband (but decaying at high wavenumbers), and it is this state that is termed wavy turbulent. Snapshots and corresponding online movies at $\alpha = 0.90$ are shown in figures 8(*d*), 9(*b*) and 9(*d*).

Repeating this exercise of considering flows at increasing α when $\omega = 0.6\pi \approx 1.885 < 2$ produces a very different picture, primarily due to the presence of inertial waves for all $\alpha > 0$; these waves propagate at an angle of $\sim 19.5°$. The azimuthal vorticity η of the basic state at $\alpha = 0.20$ is presented in various planes and projections
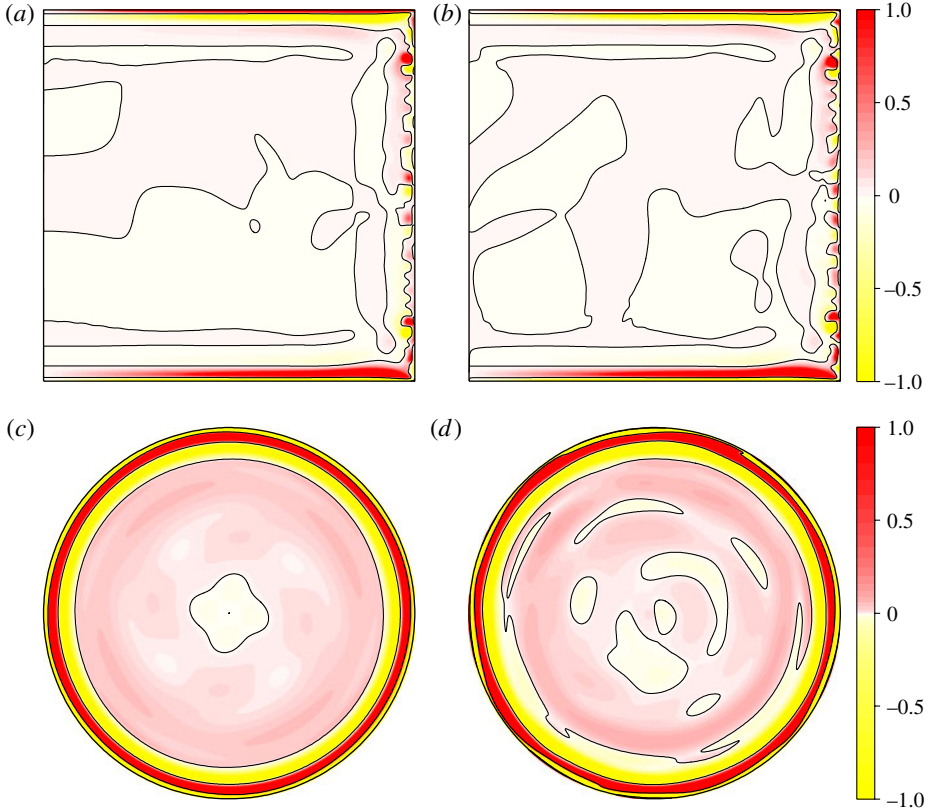
FIGURE 9. (Colour online) Azimuthal vorticity contours at $Re = 10^4$, $\gamma = 1.0$, $\omega = 0.8\pi$ with α as indicated, in a meridional section ($r \in [0.0, 1.0]$, $\theta = 0$, $z \in [0.0, 1.0]$) and a horizontal section ($r \in [0.0, 1.0]$, $\theta \in [0, 2\pi]$, $z = 0.25$). The colour bar is scaled by the maximum (red) and minimum (yellow) levels in each section, with $\eta \in [-5, 5]$ for the meridional section and $\eta \in [-0.25, 0.25]$ for the horizontal section. (enhanced online): (a) $\alpha = 0.80$; (b) $\alpha = 0.90$; and (c) $\alpha = 0.80$; (d) $\alpha = 0.90$.

in figures 10(a), 11(a) and 12(a). At this ω, the basic state becomes unstable for α greater than ~ 0.27; the bifurcating flow is a modulated rotating wave with $m = 4$ that is not Z_2 reflection symmetric, but is invariant to a Z_2 reflection composed with an azimuthal rotation of $\pi/4$, i.e. $R_{\pi/4}K_z$ (see figures 10b, 11b, 12b and the accompanying supplementary movies). This symmetry breaking appears to be associated with the inertial waves in the interior rather than instability of the boundary layers; the sidewall layer at this low α does not show evidence of Taylor–Görtler (TG) vortices.

Increasing α beyond ~ 0.37, the $m = 4$ modulated rotating wave becomes unstable, eventually settling down to an $m = 5$ modulated rotating wave. This transition has the very slow characteristics of an Eckhaus instability (Liu & Ecke 1999; Lopez *et al.* 2007). For $\alpha = 0.38$, we illustrate this type of transition where we have used the $m = 4$ state at $\alpha = 0.35$ as the initial condition. Figure 13 shows the temporal evolution of the kinetic energies in each azimuthal Fourier component of the flow,

$$E_m = \frac{1}{2} \int_{z=-1/2}^{z=1/2} \int_{r=0}^{r=\gamma} \boldsymbol{u}_m \cdot \boldsymbol{u}_m^* r \, \mathrm{d}r \, \mathrm{d}z, \qquad (4.1)$$
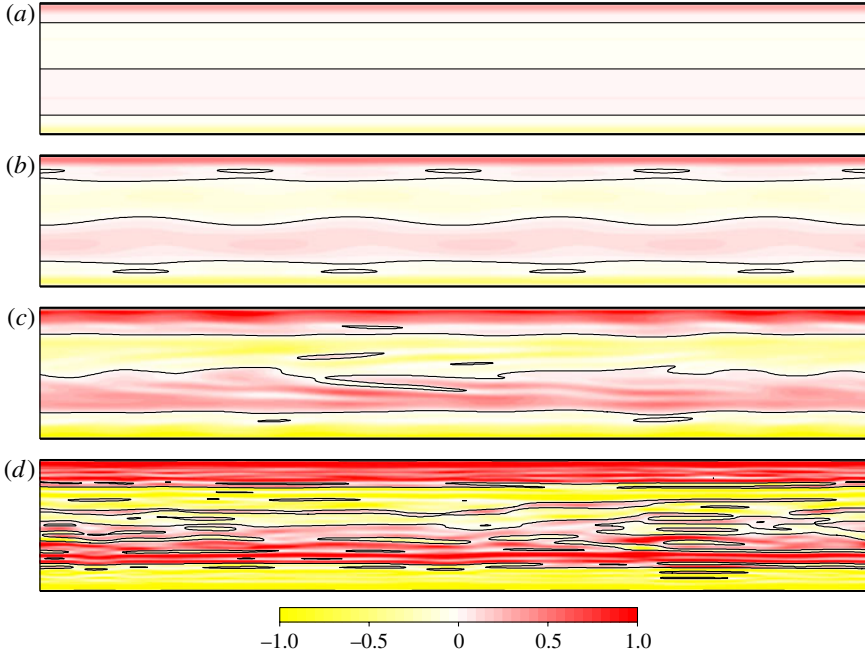
FIGURE 10. (Colour online) Azimuthal vorticity contours at $Re = 10^4$, $\gamma = 1.0$, $\omega = 0.6\pi$ with α as indicated, on the sidewall ($r = 1.0$, $\theta \in [0, 2\pi]$, $z \in [0.0, 1.0]$). The colour bar is scaled by the maximum (red) and minimum (yellow) levels of $\eta \in [-10, 10]$ (enhanced online): (a) $\alpha = 0.20$; (b) $\alpha = 0.30$; (c) $\alpha = 0.50$; and (d) $\alpha = 0.70$.

where $\boldsymbol{u}_m$ is the mth Fourier mode of the velocity field and $\boldsymbol{u}_m^*$ is its complex conjugate. The figure shows that the energies in azimuthal wavenumber $m = 4$ and its harmonics remain almost constant for about two-thirds of a viscous time (with the time scaling used, one viscous time corresponds to Re time units, which for this ω is ~ 3000 libration periods). During this time, the other modal energies are growing exponentially (linear in the log-linear plot used in the figure). Then for about a quarter of a viscous time, the flow appears to have settled into a mixed-mode state where the $m = 4$ state is modulated by $m = 2$ (like a square being alternatively squeezed along one diagonal and then the other). During this phase of the evolution, the flow components with $m = 5$ and its harmonics decay for a while, but then suddenly, at $\sim t = 10^4$, start to grow and eventually saturate whilst the other components of the flow decay, leaving a stable $m = 5$ modulated rotating wave, after about two viscous times of evolution. This very slow dynamics is typical of the flows in this study, and illustrates the computational challenges in performing a bifurcation analysis. For example, we could have computed the unstable $m = 4$ state by imposing its symmetry and then performed a linear stability analysis (this would not be a straightforward Floquet analysis as the state being investigated is not periodic, but quasiperiodic). However, such an analysis would have indicated instability to $m = 2$, and yet the nonlinear evolution just described shows that the stable bifurcating state is an $m = 5$ modulated rotating wave. In these flows, linear stability analysis does not provide a reliable prediction of what an unstable flow will saturate to.

By $\alpha = 0.5$, the sidewall boundary layer has become unstable and has TG vortices (much like those described for the $\omega = 0.8\pi$ case, but there they did not appear until α
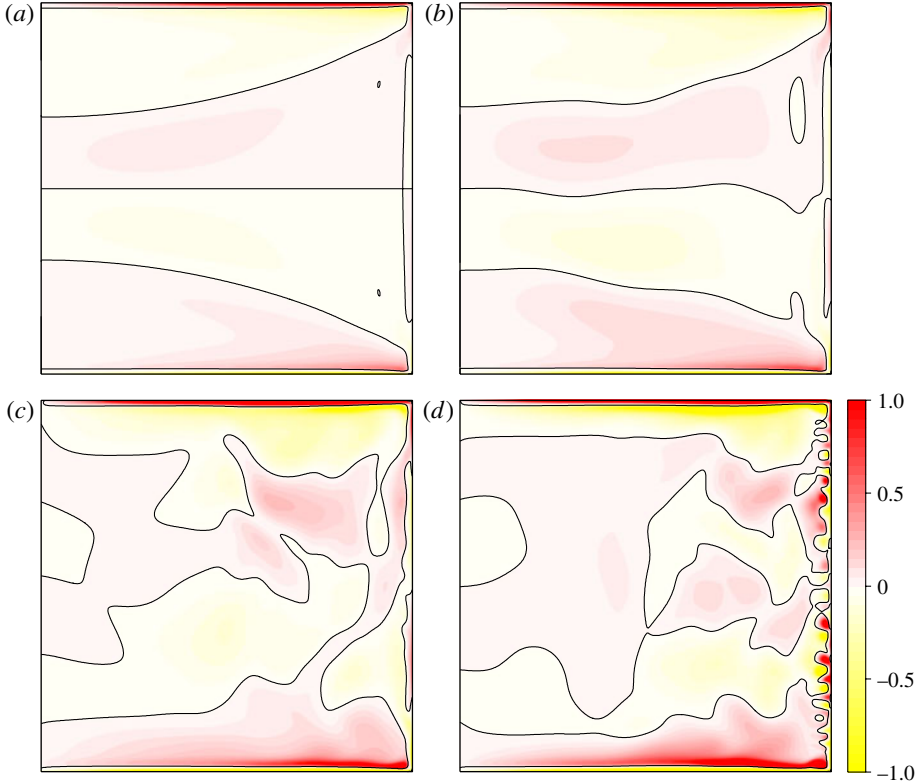
FIGURE 11. (Colour online) Azimuthal vorticity contours at $Re = 10^4$, $\gamma = 1.0$, $\omega = 0.6\pi$ with α as indicated, in a meridional section ($r \in [0.0, 1.0]$, $\theta = 0$, $z \in [0.0, 1.0]$). The colour bar is scaled by the maximum (red) and minimum (yellow) levels of $\eta \in [-5, 5]$ (enhanced online): (*a*) $\alpha = 0.20$; (*b*) $\alpha = 0.30$; (*c*) $\alpha = 0.50$; and (*d*) $\alpha = 0.70$.

was significantly larger), but these are now present in an environment with pre-existing non-axisymmetric inertial waves; the vortices and the waves interact to produce a rather complicated flow (see figures 10*c*, 11*c* and 12*c*).

Further increasing α above ~0.6 intensifies the TG vortices in the sidewall and there is a very noticeable coupling between them and the inertial waves. Figures 10(*d*), 11(*d*), 12(*d*) and the accompanying supplementary movies show the azimuthal vorticity for this flow, and the movies in particular give some hint to the extent of the coupling. However, the movies are only showing the flow over one libration period, and the coupling has a very low-frequency form characteristic of a flow near a heteroclinic cycle. Figure 14 shows the time series of E_5 and E_6, which apart from the underlying axisymmetric component, are the energies of the dominant components of this flow state. It shows that there is a fairly regular exchange of energy between the $m = 5$ and $m = 6$ components, occurring with a period of roughly 330, which corresponds to ~100 libration periods. Similar low-frequency behaviour was found for $\alpha = 0.8$ and 0.9.

The dynamics are again different for the lower libration frequency $\omega = 0.4\pi \approx 1.26$ case. Again, inertial waves are present for all $\alpha > 0$, but now they propagate at an angle of ~51°. This leads to significant undulations in the top and bottom boundary layers and in the sidewall layer. The undulations in the sidewall layer

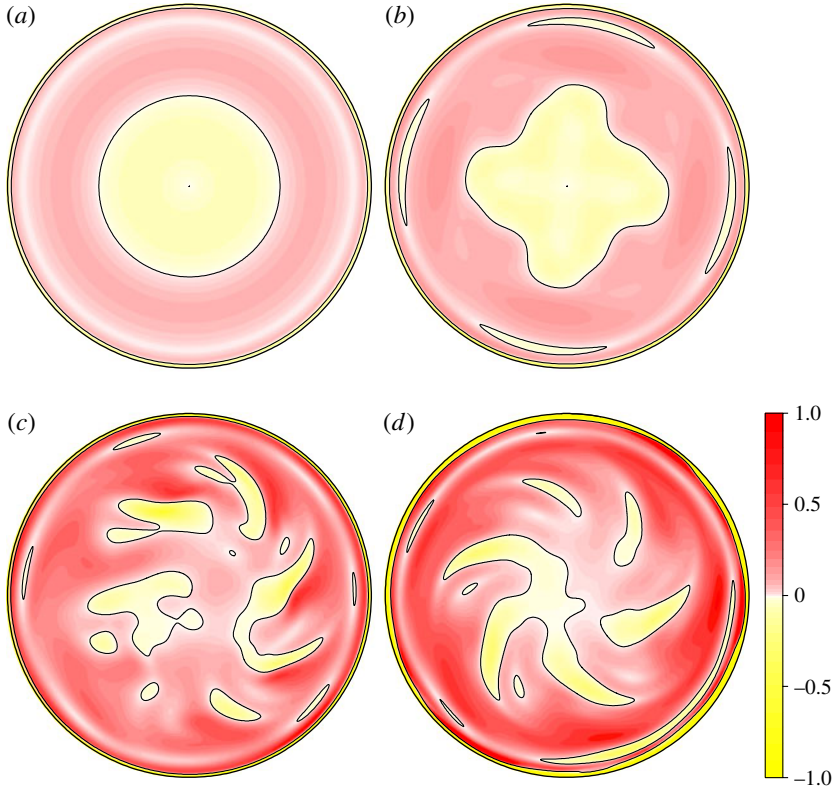FIGURE 12. (Colour online) Azimuthal vorticity contours at $Re = 10^4$, $\gamma = 1.0$, $\omega = 0.6\pi$ with α as indicated, in a horizontal section ($r \in [0.0, 1.0]$, $\theta \in [0, 2\pi]$, $z = 0.25$). The colour bar is scaled by the maximum (red) and minimum (yellow) levels $\eta \in [-2, 2]$ (enhanced online): (*a*) $\alpha = 0.20$; (*b*) $\alpha = 0.30$; (*c*) $\alpha = 0.50$; and (*d*) $\alpha = 0.70$.
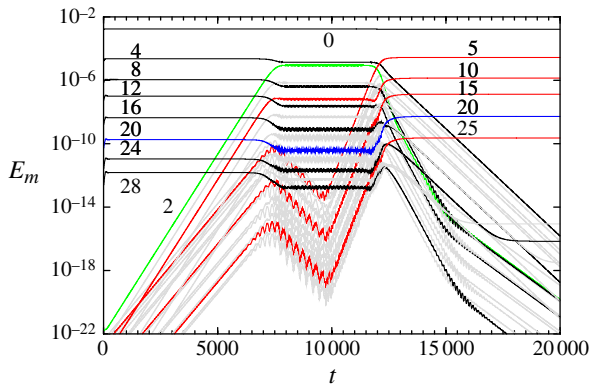

FIGURE 13. (Colour online) Time series of the modal energies for $Re = 10^4$, $\gamma = 1.0$, $\omega = 0.6\pi$ and $\alpha = 0.38$, showing a slow transition from an $m = 4$ state to an $m = 5$ state.

promote separation zones on the scale of the TG vortices we have described for the larger ω cases. Up to $\alpha = 0.51$, the flow remains $SO(2) \times Z_2$ and synchronous.
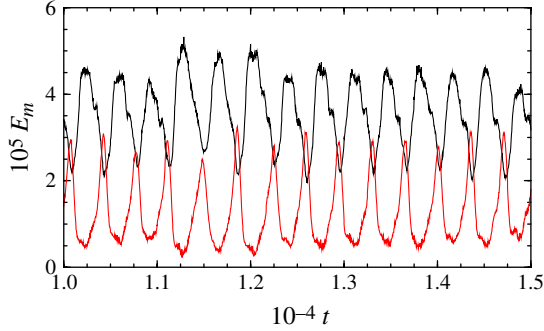
FIGURE 14. (Colour online) Time series of the modal energies E_5 (black) and E_6 (red) over half a viscous time, after the flow had evolved over one viscous time, indicative of being close to a heteroclinic cycle, for $Re = 10^4$, $\gamma = 1.0$, $\omega = 0.6\pi$ and $\alpha = 0.70$.
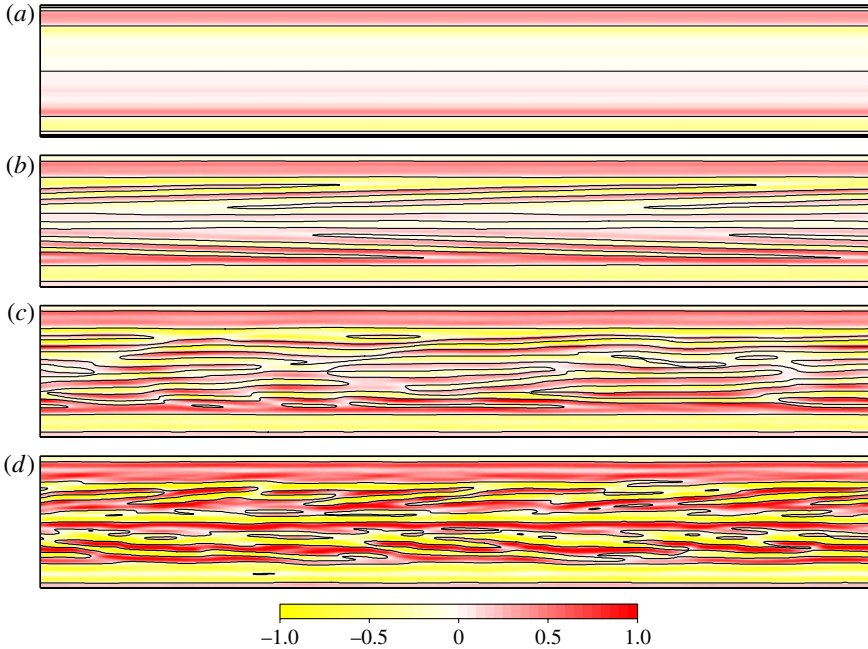

FIGURE 15. (Colour online) Azimuthal vorticity contours at $Re = 10^4$, $\gamma = 1.0$, $\omega = 0.4\pi$ with α as indicated, on the sidewall ($r = 1.0$, $\theta \in [0, 2\pi]$, $z \in [0.0, 1.0]$). The colour bar is scaled by the maximum (red) and minimum (yellow) levels of $\eta \in [-10, 10]$. (*a*) $\alpha = 0.50$; (*b*) $\alpha = 0.55$; (*c*) $\alpha = 0.60$; and (*d*) $\alpha = 0.70$.

Figures 15(*a*), 16(*a*) and 17(*a*) illustrate this flow at $\alpha = 0.50$. For $\alpha \geqslant 0.52$, the sidewall TG vortices are well-formed, but they are not primarily at the equator as they were for the larger ω cases, but rather form around $z = \pm 0.25$. For $\alpha = 0.55$, figures 15(*b*), 16(*b*) and 17(*b*) show that the flow is essentially axisymmetric, except for the TG vortices which have an azimuthal wavenumber $m = 2$ variation, and Z_2 reflection symmetric, except again for the TG vortices near the equator. By $\alpha = 0.6$, the TG vortices have clearly broken the Z_2 symmetry in the sidewall boundary layer
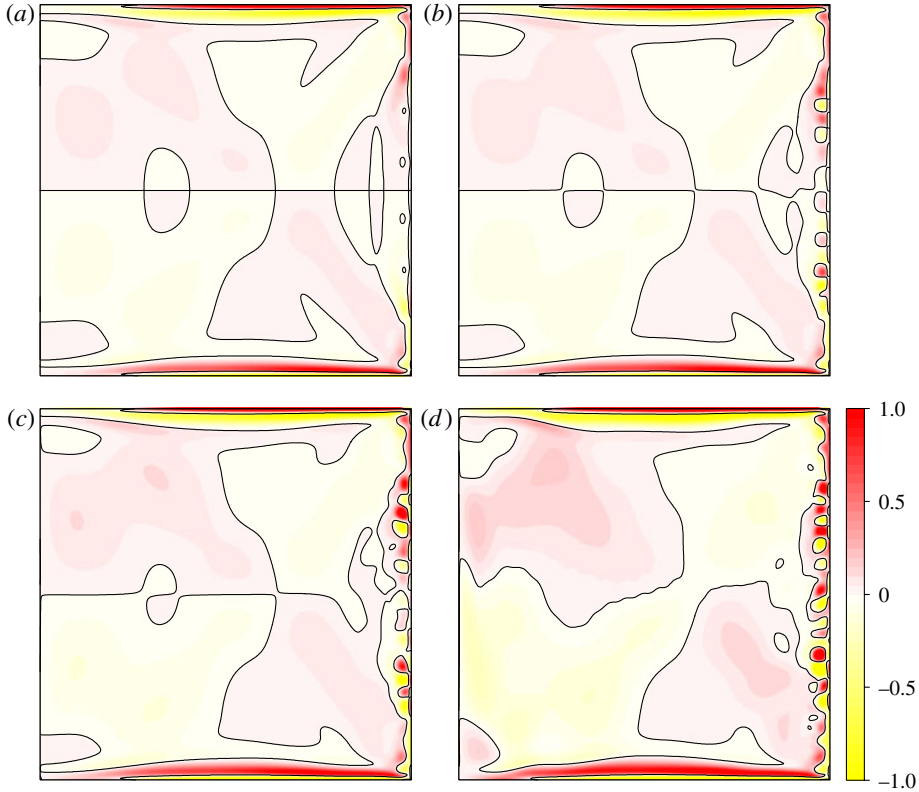
FIGURE 16. (Colour online) Azimuthal vorticity contours at $Re = 10^4$, $\gamma = 1.0$, $\omega = 0.4\pi$ with α as indicated, in a meridional section ($r \in [0.0, 1.0]$, $\theta = 0$, $z \in [0.0, 1.0]$). The colour bar is scaled by the maximum (red) and minimum (yellow) levels of $\eta \in [-5, 5]$ (enhanced online): (*a*) $\alpha = 0.50$; (*b*) $\alpha = 0.55$; (*c*) $\alpha = 0.60$; and (*d*) $\alpha = 0.70$.

region as well as becoming completely three-dimensional, but the inertial wave flow remains essentially $SO(2) \times Z_2$ (see figures 15*c*, 16*c* and 17*c*). By $\alpha = 0.7$ (see figures 15*d*, 16*d*, 17*d* and the accompanying supplementary movies) the inertial waves have also broken Z_2, but they remain essentially axisymmetric, except for close to the sidewall layer.

5. Discussion and conclusions

Inertial waves are ubiquitous in rotating fluids, but they are quickly damped and have a significant impact in the flow only when there is a permanent source that excites them. This can be the case in the presence of noise or an external periodic forcing, or even due to the intrinsic dynamics of the flow that develops non-trivial temporal behaviour triggering inertial waves (Lopez & Marques 2010). Geophysical problems have several periodic forcings and therefore there is a growing interest in inertial waves in geophysical flows, as well as in controlled laboratory experiments designed to mimic some features of geophysical flows (Kelley *et al.* 2006; Bewley *et al.* 2007; Kelley *et al.* 2007; Noir *et al.* 2009; Kelley *et al.* 2010; Calkins *et al.* 2010; Noir *et al.* 2010).
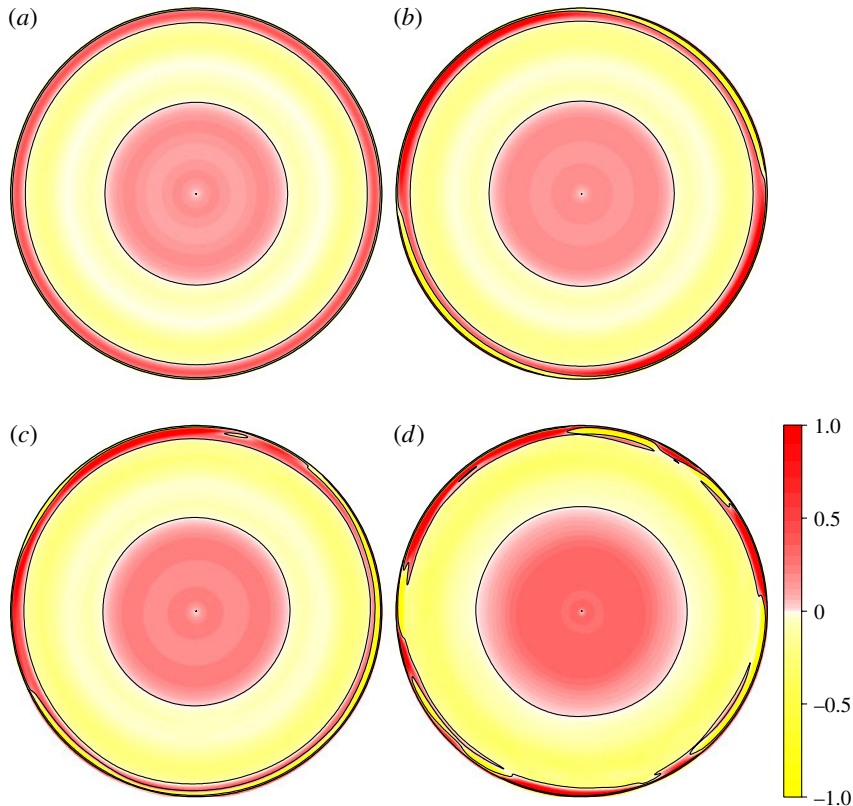
FIGURE 17. (Colour online) Azimuthal vorticity contours at $Re = 10^4$, $\gamma = 1.0$, $\omega = 0.4\pi$ with α as indicated, in a horizontal section ($r \in [0.0, 1.0]$, $\theta \in [0, 2\pi]$, $z = 0.25$). The colour bar is scaled by the maximum (red) and minimum (yellow) levels of $\eta \in [-2, 2]$ (enhanced online): (*a*) $\alpha = 0.50$; (*b*) $\alpha = 0.55$; (*c*) $\alpha = 0.60$; and (*d*) $\alpha = 0.70$.

Interactions between inertial waves (largely understood in the context of linear, inviscid dynamics) and viscous boundary and shear layer flows are observed in a variety of settings. For example, Bewley *et al.* (2007) observed in their rotating grid turbulence experiments that large-scale inertial waves quickly sensed the boundaries and they presented arguments to suggest that the resultant inhomogeneities they observed should be a general feature of rotating turbulent flows. In rotating spherical cavities, inertial waves are found to be driven by instabilities and eruptions of the Ekman layer (Noir *et al.* 2001; Noir, Jault & Cardin 2001; Lorenzani & Tilgner 2001), and in differentially rotating cylinder flow, inertial waves generated by sidewall boundary layer instability have been reported (Lopez & Marques 2010). Furthermore, rotating convection in low-Prandtl-number fluids can be interpreted as inertial waves driven by buoyancy (Zhang 1994, 1995; Busse & Simitev 2004; Zhang, Liao & Busse 2007).

In the present study we have investigated the flow in a rotating circular cylinder driven by a harmonic modulation of the rotation rate, i.e. a librating cylinder, focusing on two main points: the boundary layer structure of the base state and the subsequent bifurcations resulting in the experimentally observed 'wavy' turbulent flow.

The top and bottom boundary layer structure of the base state agrees well with the analysis developed by Wang (1970), but the sidewall boundary layer is very complex and had not been studied in detail previously. The corner regions couple the horizontal top and bottom boundary layers with the vertical sidewall boundary layer, giving rise to a LSC originating at the corners. The bulk of the fluid is in solid-body rotation for large modulation frequencies ($\omega > 2$), with a slightly retrograde precession with respect to the mean rotation rate of the container. However, for small modulation frequencies ($\omega < 2$) inertial waves are excited, regardless of the size of the modulation amplitude α, and these drastically change the properties of the base state, driving the bulk flow away from solid-body rotation, establishing a time-dependent flow throughout the entire cylinder and strongly modifying the boundary layers that are now less intense. We have also found that inertial waves can be excited, even with $\omega > 2$, via an axisymmetric period-doubling instability of the sidewall that produces a flow with a frequency smaller than two, thus allowing the generation of inertial waves.

When the base state becomes unstable to three-dimensional perturbations, a complex succession of secondary instabilities takes place over a small range of α, resulting in states with all symmetries broken and broad-band temporal characteristics, that closely resemble the wavy turbulent states observed in experiments (Noir *et al.* 2010). The route to spatiotemporal complexity in this problem is highly dependent on the value of the modulation amplitude and on the presence and angle of propagation of the inertial waves. When the modulation frequency is large ($\omega > 2$) the instabilities develop near the centre of the sidewall boundary layer, in the form of TG vortices, generating herringbone patterns of increasing complexity with increasing α, breaking all of the symmetries of the problem and evolving towards wavy turbulence. Inertial waves are absent or very weak, and the dynamics is concentrated on and near the boundary layers.

When the modulation frequency is smaller but close to the threshold of inertial waves ($\omega \lesssim 2$) we find a very different picture due to the presence of inertial waves filling the fluid domain. The bifurcated flows are modulated rotating waves, and the symmetry-breaking process appears to be associated with the inertial waves in the interior rather than instability of the boundary layers, that do not show evidence of TG vortices. Modulated rotating waves with different azimuthal wavenumbers compete in a way similar to the Eckhaus instability, with very slow dynamics. Further increasing α results in the formation of TG vortices that couple with the inertial waves resulting in heteroclinic-type dynamics.

For a lower modulation frequency, the inertial waves have a larger inclination angle producing significant undulations in all of the boundary layers. Now the TG vortices form midway between the equator and the top and bottom lids. The flow remains nearly axisymmetric in the bulk, except close to the sidewall layer, where the dynamics becomes very complex, similar to wavy turbulence.

This first study on the interaction between boundary layers and inertial waves and the development of wavy turbulence in a librating cylinder can be reasonably easily reproduced and analysed in laboratory experiments. Such experiments would be able to cover a larger parameter range, and they are essential to confirm the findings of the present study and potentially uncover further new dynamics. Previous experiments, that have been very useful, focused on partial aspects of the problem, and the strong interaction between boundary layers and inertial waves, filling the whole flow domain, requires additional and more comprehensive experiments.

There are many open questions in the present problem, and a few of them deserve explicit mention here. One open question is what happens at larger *Re* numbers, with

large mean rotation rates and very thin boundary layers: what are the changes in the flow dynamics and the wave turbulence? Another open question is the detailed response of the system to different modulation frequencies (we have explored only three frequencies in this study), and if there are critical frequencies or frequency intervals where the response is particularly intense, as occurs in similar problems involving thin boundary layers in rotating flows that are periodically forced (Do *et al.* 2010).

Supplementary movies are available at journals.cambridge.org/flm.

REFERENCES

ALDRIDGE, K. D. & LUMB, L. I. 1987 Inertial waves identified in the Earth's fluid outer core. *Nature* **325**, 421–423.

ALDRIDGE, K. D. & TOOMRE, A. 1969 Axisymmetric inertial oscillations of a fluid in a rotating spherical container. *J. Fluid Mech.* **37**, 307–323.

BARCILON, V. 1968 Stewartson layers in transient rotating fluid flows. *J. Fluid Mech.* **33**, 815–825.

BARRETT, K. E. 1969 Resonant torsional oscillations of a pair of discs in a rotating fluid. *Z. Angew. Math. Phys.* **20**, 721–729.

BENNEY, D. J. 1965 The flow induced by a disk oscillating about a state of steady rotation. *Q. J. Mech. Appl. Maths* **18**, 333–345.

BEWLEY, G. P., LATHROP, D. P., MAAS, L. R. M. & SREENIVASAN, K. R. 2007 Inertial waves in rotating grid turbulence. *Phys. Fluids* **19**, 071701.

BHATTACHARJEE, J. K. 1989 Rotating Rayleigh–Bénard convection with modulation. *J. Phys.* A **22**, L1135–L1139.

BHATTACHARJEE, J. K. 1990 Convective instability in a rotating fluid layer under modulation of the rotating rate. *Phys. Rev.* A **41**, 5491–5494.

BUSSE, F. H. 2010a Mean zonal flows generated by librations of a rotating spherical cavity. *J. Fluid Mech.* **650**, 505–512.

BUSSE, F. H. 2010b Zonal flow induced by longitudinal librations of a rotating cylindrical cavity. *Physica* D **240**, 208–211.

BUSSE, F. H. & SIMITEV, R. 2004 Inertial convection in rotating fluid spheres. *J. Fluid Mech.* **498**, 23–30.

CALKINS, M. A., NOIR, J., ELDREDGE, J. D. & AURNOU, J. M. 2010 Axisymmetric simulations of libration-driven fluid dynamics in a spherical shell geometry. *Phys. Fluids* **22**, 086602.

DO, Y., LOPEZ, J. M. & MARQUES, F. 2010 Optimal harmonic response in a confined Bödewadt boundary layer flow. *Phys. Rev.* E **82**, 036301.

GREENSPAN, H. P. 1968 *The Theory of Rotating Fluids*. Cambridge University Press.

GREENSPAN, H. & HOWARD, L. 1963 On a time-dependent motion of a rotating fluid. *J. Fluid Mech.* **17**, 385–404.

HART, J. E. & MUNDT, M. D. 1996 Instability of oscillatory Stokes–Stewartson layers in a rotating fluid. *J. Fluid Mech.* **311**, 119–140.

JONES, A. F. 1969 The resonance effect of a disk oscillating about a state of steady rotation. *J. Fluid Mech.* **39**, 269–281.

KELLEY, D. H., TRIANA, S. A., ZIMMERMAN, D. S., BRAUN, B., LATHROP, D. P. & MARTIN, D. H. 2006 Driven inertial waves in spherical Couette flow. *Chaos* **16**, 041105.

KELLEY, D. H., TRIANA, S. A., ZIMMERMAN, D. S. & LATHROP, D. P. 2010 Selection of inertial modes in spherical Couette flow. *Phys. Rev.* E **81**, 026311.

KELLEY, D. H., TRIANA, S. A., ZIMMERMAN, D. S., TILGNER, A. & LATHROP, D. P. 2007 Inertial waves driven by differential rotation in a planetary geometry. *Geophys. Astrophys. Fluid Dyn.* **101**, 469–487.

LANDAU, L. D. & LIFSHITZ, E. M. 1984 *Fluid Mechanics*, 2nd edn. Pergamon Press.

LIU, Y. & ECKE, R. E. 1999 Nonlinear travelling waves in rotating Rayleigh–Bénard convection: stability boundaries and phase diffusion. *Phys. Rev.* E **59**, 4091–4105.

LOPEZ, J. M. & MARQUES, F. 2009 Centrifugal effects in rotating convection: nonlinear dynamics. *J. Fluid Mech.* **628**, 269–297.

LOPEZ, J. M. & MARQUES, F. 2010 Sidewall boundary layer instabilities in a rapidly rotating cylinder driven by a differentially co-rotating lid. *Phys. Fluids* **22**, 114109.

LOPEZ, J. M., MARQUES, F., MERCADER, I. & BATISTE, O. 2007 Onset of convection in a moderate aspect-ratio rotating cylinder: Eckhaus–Benjamin–Feir instability. *J. Fluid Mech.* **590**, 187–208.

LOPEZ, J. M., MARQUES, F., RUBIO, A. M. & AVILA, M. 2009 Crossflow instability of finite Bödewadt flows: transients and spiral waves. *Phys. Fluids* **21**, 114107.

LORENZANI, S. & TILGNER, A. 2001 Fluid instabilities in precessing spheroidal cavities. *J. Fluid Mech.* **447**, 111–128.

MARQUES, F., MERCADER, I., BATISTE, O. & LOPEZ, J. M. 2007 Centrifugal effects in rotating convection: axisymmetric states and three-dimensional instabilities. *J. Fluid Mech.* **580**, 303–318.

MERCADER, I., BATISTE, O. & ALONSO, 2010 An efficient spectral code for incompressible flows in cylindrical geometries. *Comput. Fluids* **39**, 215–224.

NIEMELA, J. J., SMITH, M. R. & DONNELLY, R. J. 1991 Convective instability with time-varying rotation. *Phys. Rev.* A. **44**, 8406–8409.

NOIR, J., BRITO, D., ALDRIDGE, K. & CARDIN, P. 2001 Experimental evidence of inertial waves in a precessing spherical cavity. *Geophys. Res. Lett.* **28**, 3785–3788.

NOIR, J., CALKINS, M. A., CANTWELL, J. & AURNOU, J. M. 2010 Experimental study of libration-driven zonal flows in a straight cylinder. *Phys. Earth Planet. Inter.* **182**, 98–106.

NOIR, J., HEMMERLIN, F., WICHT, J., BACA, S. M. & AURNOU, J. M. 2009 An experimental and numerical study of librationally driven flow in planetary cores and subsurface oceans. *Phys. Earth Planet. Inter.* **173**, 141–152.

NOIR, J., JAULT, D. & CARDIN, P. 2001 Numerical study of the motions within a slowly precessing sphere at low Ekman number. *J. Fluid Mech.* **437**, 283–299.

ROXIN, A. & RIECKE, H. 2002 Rotating convection in an anisotropic system. *Phys. Rev.* E **65**, 046219.

RUBIO, A., LOPEZ, J. M. & MARQUES, F. 2008 Modulated rotating convection: radially travelling concentric rolls. *J. Fluid Mech.* **608**, 357–378.

RUBIO, A., LOPEZ, J. M. & MARQUES, F. 2009 Interacting oscillatory boundary layers and wall modes in modulated rotating convection. *J. Fluid Mech.* **625**, 75–96.

SAURET, A., CÉBRON, D., MORIZE, C. & LE BARS, M. 2010 Experimental and numerical study of mean zonal flows generated by librations of a rotating spherical cavity. *J. Fluid Mech.* **662**, 260–268.

SCHLICHTING, H. & GERSTEN, K. 2000 *Boundary-Layer Theory*, eighth edn. McGraw-Hill.

THOMPSON, K. L., BAJAJ, K. M. S. & AHLERS, G. 2002 Travelling concentric-roll patterns in Rayleigh–Bénard convection with modulated rotation. *Phys. Rev.* E **65**, 04618.

WANG, C.-Y. 1970 Cylindrical tank of fluid oscillating about a state of steady rotation. *J. Fluid Mech.* **41**, 581–592.

YIH, C.-S. 1977 *Fluid Mechanics*. West River Press.

ZATMAN, S. & BLOXHAM, J. 1997 Torsional oscillations and the magnetic field within the Earth's core. *Nature* **388**, 760–763.

ZHANG, K. 1994 On coupling between the Poincaré equation and the heat equation. *J. Fluid Mech.* **268**, 211–229.

ZHANG, K. 1995 On coupling between the Poincaré equation and the heat equation: non-slip boundary condition. *J. Fluid Mech.* **284**, 239–256.

ZHANG, K., LIAO, Z. & BUSSE, F. H. 2007 Asymptotic theory of inertial convection in a rotating cylinder. *J. Fluid Mech.* **575**, 449–471.